AIAA JOURNAL
Vol. 41, No. 1, January 2003

Technical Notes

TECHNICAL NOTES are short manuscripts describing new developments or important results of a preliminary nature. These Notes cannot exceed six manuscript pages and three figures; a page of text may be substituted for a figure and vice versa. After informal review by the editors, they may be published within a few months of the date of receipt. Style requirements are the same as for regular contributions (see inside back cover).

Viscous Supersonic Flow over Moving Compression Ramp

S. O. Park,* C. H. Lee,† and K. M. Kang‡
Korea Advanced Institute of Science and Technology, Taejon 305-701, Republic of Korea

Introduction

TWO-DIMENSIONAL, steady, inviscid, supersonic flow past a compression ramp is well understood as found in standard textbooks of gasdynamics. Unsteady flow past a moving compression ramp with time-varying wedge angle, however, has received scant attention and is, thus, little understood. In spite of a simple flow configuration, the unsteadiness of the flow defies analytical approach. Degani and Steger[1] studied numerically the compression ramp flow when the ramp angle moved from 15 to 24 deg at a constant angular velocity. In that work, the main interest was the comparison between the thin-layer and the Navier–Stokes solutions. In earlier work,[2] the inviscid, unsteady flow past a moving compression ramp was investigated numerically. Formation of a shock wave, the pressure buildup and relaxation, and the hysteresis during the ramp motion were discussed. Coon and Chapman[3] conducted an experimental study of the unsteady, three-dimensional turbulent flow over an oscillating flap at Mach 2.4. Various flow regimes and characteristics, depending on the flap angle and the frequency of oscillation, were identified and discussed. Compressible subsonic or transonic flows around an oscillating airfoil has been studied by several investigators, as can be found in Ref. 4. The unsteady characteristics of these flows are qualitatively similar to those of the present flow to be investigated. As an extension of earlier work[2] on inviscid flow, the present work was undertaken to examine viscous effect. The wedge angle varies linearly with time from 0 deg to a given wedge angle. During the ramp motion, the flowfield depends strongly on the angular velocity of the ramp at a given freestream Mach number. When the ramp motion ceases, the transient flow gradually relaxes to the steady state. If the ramp oscillates, the flow exhibits hysteretic behavior. These features will be significantly affected by the action of viscosity. Distinctly different from the Euler flow, the Navier–Stokes flow involves the separation bubble around the compression corner because of the adverse pressure gradient imposed by the shock wave. It is likely that the unsteady development of the separation bubble dictates the outer flow. The present study aims to elucidate the effect of the separation bubble on the unsteady development of the flow. We carry out a parametric study to investigate the effects of the Reynolds number and the angular velocity on the flow establishment at Mach 3. Specifically, three different Reynolds numbers based on unit length, $Re/\mathrm{m} = 10^4$, 10^5, and 10^6, and two different angular velocities, $\bar{\Omega} = 0.01$ and 0.1, are considered. The reduced angular velocity $\bar{\Omega}$ is defined by $\bar{\Omega} = \Omega L/U$, where Ω is the angular velocity of the ramp motion, L the reference length of 1 m, and U the freestream velocity.

Computational Details

The two-dimensional, unsteady Navier–Stokes equations in conservation form for general coordinate system can be written as[5]

$$\frac{\partial}{\partial t}\left(\frac{\boldsymbol{Q}}{J}\right) + \frac{\partial(\hat{\boldsymbol{F}} - \hat{\boldsymbol{F}}_v)}{\partial \xi} + \frac{\partial(\hat{\boldsymbol{G}} - \hat{\boldsymbol{G}}_v)}{\partial \eta} = 0 \tag{1}$$

The details of the various vectors in Eq. (1) are to be found in Ref. 5. The moving grid velocity is automatically taken into account in the contravariant velocity. Using a finite volume method, we obtain the following semidiscrete conservation approximation of Eq. (1) with unit spacing $\Delta\xi = 1$ and $\Delta\eta = 1$:

$$\left(\frac{1}{J}\frac{\partial \boldsymbol{Q}}{\partial \boldsymbol{t}}\right)_{i,j} + (\tilde{\boldsymbol{F}} - \tilde{\boldsymbol{F}}_v)_{i+\frac{1}{2},j} - (\tilde{\boldsymbol{F}} - \tilde{\boldsymbol{F}}_v)_{i-\frac{1}{2},j} + (\tilde{\boldsymbol{G}} - \tilde{\boldsymbol{G}}_v)_{i,j+\frac{1}{2}} - (\tilde{\boldsymbol{G}} - \tilde{\boldsymbol{G}}_v)_{i,j-\frac{1}{2}} = 0 \tag{2}$$

For unsteady time-accurate calculations of Eq. (2), we adopt the subiteration time-advance scheme of Pulliam,[6] which is formulated as

$$\left[\frac{\boldsymbol{I}}{J\Delta t} + \frac{\vartheta}{1+\varphi}\left(\frac{\partial \boldsymbol{R}(\boldsymbol{Q}^p)}{\partial \boldsymbol{Q}}\right)\right](\boldsymbol{Q}^{p+1} - \boldsymbol{Q}^p) = -\frac{1}{1+\varphi}\boldsymbol{R}(\boldsymbol{Q}^p) - \frac{1}{J\Delta t}\left[\boldsymbol{Q}^p - \frac{1+2\varphi}{1+\varphi}\boldsymbol{Q}^n + \frac{\varphi}{1+\varphi}\boldsymbol{Q}^{n-1}\right] \tag{3}$$

where $\boldsymbol{Q}^p$ and $\boldsymbol{Q}^{p+1}$ are the solutions of the subiteration level and $\boldsymbol{Q}^n$ and $\boldsymbol{Q}^{n-1}$ are the solutions of previous time levels. The solution at time level $n+1$ is taken from the converged solution $\boldsymbol{Q}^{p+1}$. In this study, we take $\vartheta = 1$ and $\varphi = \frac{1}{2}$, which gives the three-point backward implicit scheme to result in second-order accuracy in time.

The residual vector $\boldsymbol{R}(\boldsymbol{Q})$ of the right-hand side (RHS) of Eq. (3) is given as

$$\boldsymbol{R}(\boldsymbol{Q}) = (\tilde{\boldsymbol{F}} - \tilde{\boldsymbol{F}}_v)_{i+\frac{1}{2},j} - (\tilde{\boldsymbol{F}} - \tilde{\boldsymbol{F}}_v)_{i-\frac{1}{2},j} + (\tilde{\boldsymbol{G}} - \tilde{\boldsymbol{G}}_v)_{i,j+\frac{1}{2}} - (\tilde{\boldsymbol{G}} - \tilde{\boldsymbol{G}}_v)_{i,j-\frac{1}{2}} \tag{4}$$

For the calculation of inviscid fluxes, $\tilde{\boldsymbol{F}}$ and $\tilde{\boldsymbol{G}}$, Roe's[7] approximate Riemann solver is used. High-order accuracy in space is achieved with the MUSCL approach,[8] and primitive variables are extrapolated to the cell interface with the Van Albada limiter function. The viscous fluxes, $\tilde{\boldsymbol{F}}_v$ and $\tilde{\boldsymbol{G}}_v$, are discretized by the central difference. For the calculation of Jacobian matrices, $\partial \boldsymbol{R}/\partial \boldsymbol{Q}$, of the implicit part of Eq. (3), we use the first-order Steger–Warming's flux vector splitting scheme for inviscid fluxes, and retain only nonmixed derivative

Presented as Paper 2001-0568 at the 39th Aerospace Sciences Meeting, Reno, NV, 8–11 January 2001; received 26 June 2001; revision received 19 August 2002; accepted for publication 26 August 2002. Copyright © 2002 by the American Institute of Aeronautics and Astronautics, Inc. All rights reserved. Copies of this paper may be made for personal or internal use, on condition that the copier pay the $10.00 per-copy fee to the Copyright Clearance Center, Inc., 222 Rosewood Drive, Danvers, MA 01923; include the code 0001-1452/03 $10.00 in correspondence with the CCC.

*Professor, Department of Aerospace Engineering, 373-1 Kusong-dong, Yusong-gu; sopark@kaist.ac.kr. Senior Member AIAA.

†Graduate Student, Department of Aerospace Engineering; currently Senior Researcher, Smart UAV Development Center, Korea Aerospace Research Institute, Taejon 305-333, Republic of Korea.

‡Graduate Student, Department of Aerospace Engineering; currently Engineer, T-50 Aerodynamics Team, Korea Aerospace Industries, Ltd., Sacheon 664-940, Republic of Korea.

terms for viscous fluxes. Thus, the residual vector at point (i, j) in the implicit part is dependent on the states of four neighboring grid points. The resulting matrix equation at the point (i, j) can be written as

$$\boldsymbol{C}_1 \Delta \boldsymbol{Q}^n_{i,j} + \boldsymbol{C}_2 \Delta \boldsymbol{Q}^n_{i-1,j} + \boldsymbol{C}_3 \Delta \boldsymbol{Q}^n_{i,j-1} + \boldsymbol{C}_4 \Delta \boldsymbol{Q}^n_{i+1,j} + \boldsymbol{C}_5 \Delta \boldsymbol{Q}^n_{i,j+1} = -\mathrm{RHS} \tag{5}$$

where each of $\boldsymbol{C}_1, \ldots, \boldsymbol{C}_5$ represents coefficient matrix composed of Jacobians. The RHS of Eq. (5) is the same as that of Eq. (3). To solve Eq. (5), we adopt the point symmetric Gauss–Seidel scheme. In this approach, terms with coefficients $\boldsymbol{C}_2, \ldots, \boldsymbol{C}_5$ in the left-hand side of Eq. (5) are moved to the RHS, and hence, only the inversion of $\boldsymbol{C}_1$ becomes necessary. For each subiteration level, the computation is carried out in forward and backward sweeps.

Results and Discussion

Code Validation with Steady Flow

To validate the code used in the present work, we first calculated the steady flow studied experimentally by Lewis et al.[9] The flow conditions were wedge angle equal to 10.25 deg, $M_\infty = 6.06$, $T_\infty = 50$ K, $T_w/T_{0\infty} = 0.2$, and $Re_{x_c} = 1.5 \times 10^5$, 3.0×10^5, and 5.0×10^5. The Reynolds number was based on the length from the leading edge of the plate to the compression corner, which was 2.5 in. (6.35 cm). Three different Reynolds numbers were realized by varying the stagnation pressure with the stagnation temperature fixed.

A grid dependency test was carried out as shown in Fig. 1a to ensure a grid independent solution at $Re_{x_c} = 5.0 \times 10^5$. The computational domain covered the region from the station of 0.25 in. (0.635 cm) ahead of the leading edge to the station of 2.5 in. (6.35 cm) from the corner in the streamwise direction and from the wall to about 20 times the boundary-layer thickness at the midpoint of the flat plate in the transverse direction. At the inlet plane [0.25 in. (0.635 cm) ahead of the leading edge], the uniform velocity was specified. As can be seen in Fig. 1a, the 281×121 grid yielded essentially the same solution as the 561×241 grid. Hence, the 281×121 grid was used to validate the code. Figure 1b compares the experimental data with the present computational data. We see that the pressure ahead of the corner is underpredicted in all of the three cases. We conjecture that this is due to the leading-edge shock. In the experiment, the leading edge must be of finite thickness to result in a stronger leading-edge shock, whereas it is of zero thickness in the present computation. (The information about the leading edge geometry was unavailable.) The weaker leading-edge shock of the computation necessarily results in lower pressure, as seen in Fig. 1b. The tendency of the pressure variation with the Reynolds number, however, is in good agreement with the experimental data. The increase of the upstream influence, the increase of the separation bubble size with the Reynolds number, and the decrease of the pressure over the plate with the increasing Reynolds number are well reproduced in the computational results. These effects of the Reynolds number on the supersonic compression ramp flow are well established through the triple deck theory where the ramp angle scales as $\mathrm{Re}^{1/4}\theta$ (Refs. 10 and 11).

Unsteady Flow

The wedge angle varies linearly from 0 to 10 deg at constant angular velocity. We first look into the case when the ramp moves upward to 10-deg wedge angle and then stops impulsively at that angle. Later, we investigate the case when the ramp undergoes 0–10–0 deg cyclic motion. The flow conditions are $M_\infty = 3.0$, $T_\infty = 300$ K, and $Re = 10^4$, 10^5, and 10^6. The Reynolds number is based on unit length. Variation of the Reynolds number is achieved by specifying the freestream pressure with the temperature fixed; the corresponding pressures are $p_\infty = 15.267$, 152.67, and 1526.7 N/m^2, respectively. The computational domain consists of the region covering a 0.8 unit length upstream of the corner and a 1.6 unit length downstream of the corner in the streamwise direction and from the wall to about 20 times the boundary-layer thickness of the flat plate of 0.2 unit length at $Re = 10^4$ in the transverse direction. The details of the grid arrangement and the result of the grid test may be found in Ref. 12. At the inlet plane, the boundary-layer solution for the flat plate of 0.2 unit length at each Reynolds number is specified.

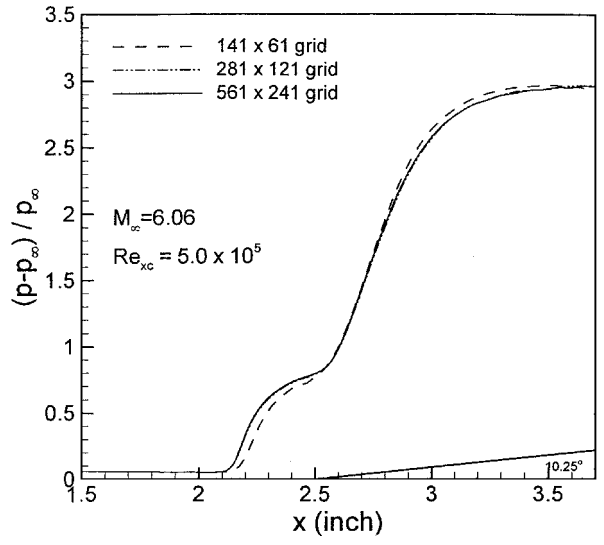

a) Effect of grid resolution

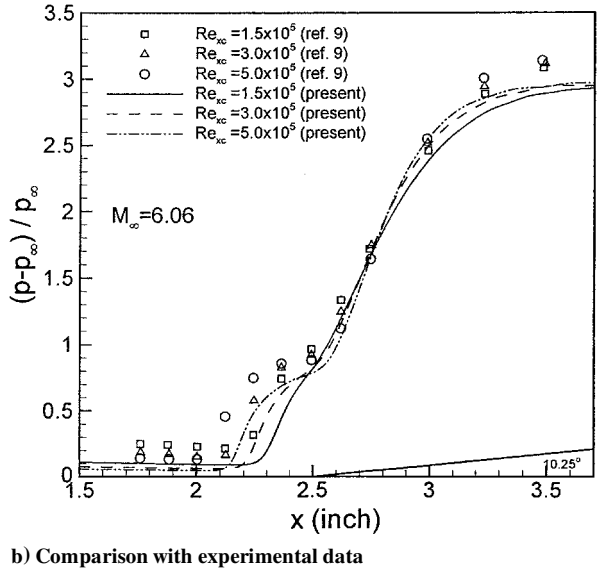

b) Comparison with experimental data

Fig. 1 Surface pressure distributions for steady ramp flow.

The unsteady flow development is well illustrated by the isopressure contours as given in Fig. 2. In Fig. 2, T is the time for the ramp to reach the final wedge angle. When the ramp moves slowly (Fig. 2a; $\bar{\Omega} = 0.01$), the shock wave formation proceeds in a manner similar to the steady flow other than the isopressure lines emanating from the moving wall. After the ramp motion ceases, we find that the region of uniform pressure has been formed above the wedge ($t = 1.1T$). The flow then gradually relaxes to that of the steady flow ($t = 2T$) with a larger separation bubble. When $\bar{\Omega} = 0.1$ (Fig. 2b), the formation of shock wave is drastically different from the case of $\bar{\Omega} = 0.01$. Because the ramp motion is very fast, isopressure lines are curved toward the moving wall. An interesting feature is observed right after the ramp stop ($t = 1.1T$). The isopressure contour for this case indicates that a local pressure maximum exists behind a curved shock. Because of the impulsive stop of the ramp, the wall pressure suddenly drops just after the stop, and hence, the already built-up high pressure forms a local pressure peak somewhere above the wall. This peculiar pressure field further develops to conform to the now steady ramp until the steady state is achieved; the pressure contour for the steady flow is shown in the plate for $t = 8.0T$.

The pressure relaxation beyond the ramp stop at the final wedge angle is given in Fig. 3. Here, s is the coordinate along the wall from the corner. Beyond the ramp stop, the angular velocity is no longer a

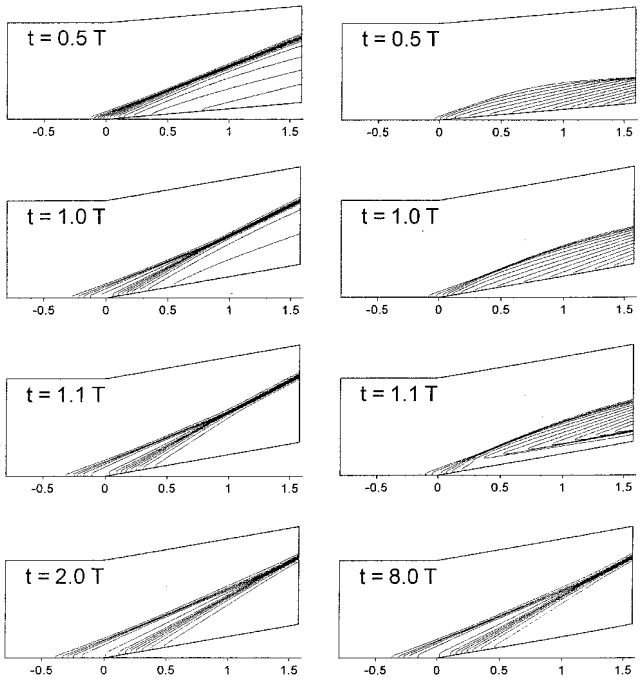

a) $\bar{\Omega} = 0.01$ b) $\bar{\Omega} = 0.1$

Fig. 2 Sequential isopressure contours, $Re = 10^5$.

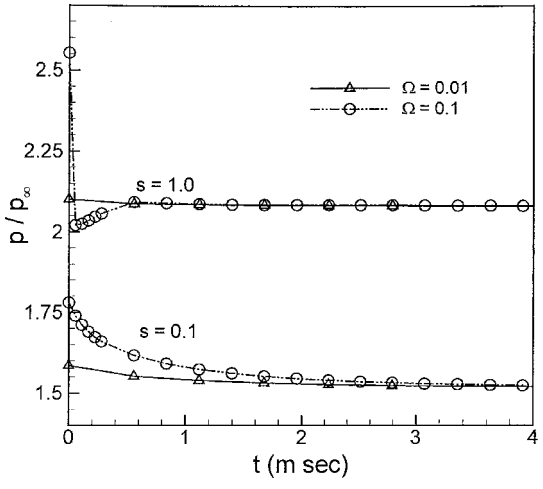

Fig. 3 Effect of $\bar{\Omega}$ on the pressure variation after ramp stop, $Re = 10^5$.

significant variable for the pressure relaxation. Hence, the pressure variation is given in terms of physical time. Figure 3 suggests that the pressure at $s = 0.1$ (near the corner) takes much longer time to settle to the steady value than the pressure at $s = 1.0$. Evidently, this is associated with the separation bubble. The pressure at $s = 1.0$ essentially behaves as the inviscid pressure. The time (measured after the ramp stop) taken for the pressure at $s = 1.0$ to assume the steady value was found to be essentially independent of the Reynolds number. However, at $s = 0.1$, the relaxation time was found to be strongly dependent on the Reynolds number. It took much longer for the pressure to settle to the steady value when the Reynolds number was large. The flow behavior near the corner, associated with the separation bubble, prevents us from categorizing the overall flow to be quasi steady even when the reduced angular velocity is very small in contrast to the Euler flow where the flow was quasi steady[2] when $\bar{\Omega} = 0.01$. This unsteady nature at a small reduced frequency was also noticed in Coon and Chapman's oscillating flap experiment.[3]

When the ramp undergoes 0–10–0-deg cyclic motion, the flow naturally exhibits hysteretic behavior. Figure 4 displays surface pressure variation at two different points during the cycle. Also shown in

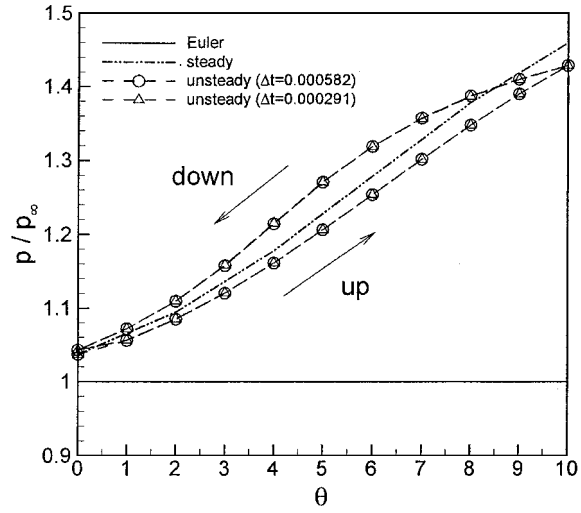

a) $s = -0.028$

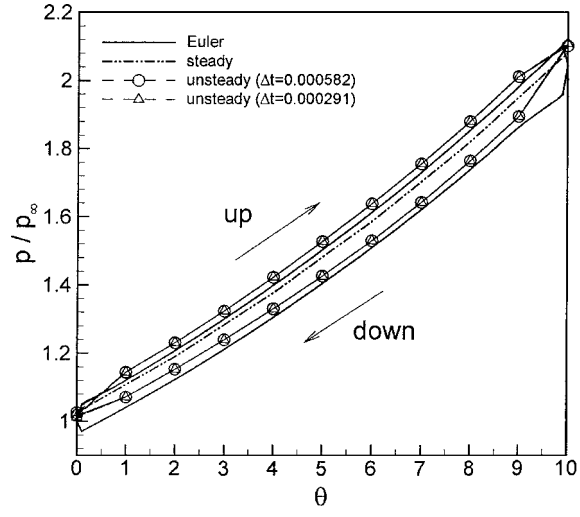

b) $s = 1.0$

Fig. 4 Surface pressure variation with wedge angle, $\bar{\Omega} = 0.01$ and $Re = 10^5$.

Fig. 4 is the effect of time step on the computational result. The time step was chosen based on the dimensionless time $T = \theta_{\max}/(M_\infty \bar{\Omega})$ for each case. The time step Δt was set to be $T/10{,}000$, which approximately corresponds to the maximum Courant–Friedrichs–Levy number of 23 when $\bar{\Omega} = 0.01$ and 2.3 when $\bar{\Omega} = 0.1$. To ensure that this time step was sufficiently small, we also performed the calculation with $0.5\Delta t$. As shown in Fig. 4, the solution with Δt coincides with the solution with $0.5\Delta t$ indicating that the present time step is indeed adequate. Figure 4a compares the pressure change with wedge angle (or equivalently time) at the point of $s = -0.028$ (the point just ahead of the corner) during the cycle. For the Euler flow, the pressure at this point does not vary with the wedge angle because there is no upstream influence. During the upward ramp motion, the pressure increasing with the wedge angle is smaller than the corresponding steady value. However, during the downward motion, the pressure is greater than the steady value exemplifying the hysteretic behavior. The higher pressure realized in the downward phase signifies that the shock stem affecting the viscous region is stronger in the downward phase than in the upward phase. The pressure variation at $s = 1.0$ (point farther away from the corner) is illustrated in Fig. 4b. As can be expected, the pressure variation during the cycle is similar to that of the Euler solution. During the upward ramp motion, the pressure is higher than the corresponding steady value, and during the downward motion, it is smaller than the steady value reflecting the motion of the ramp. Thus, we see that the pressure variation in the close vicinity of the corner is qualitatively

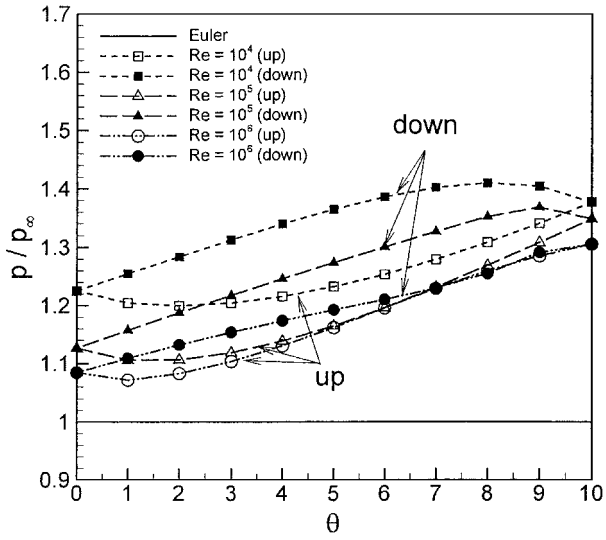

a) $s = -0.028$

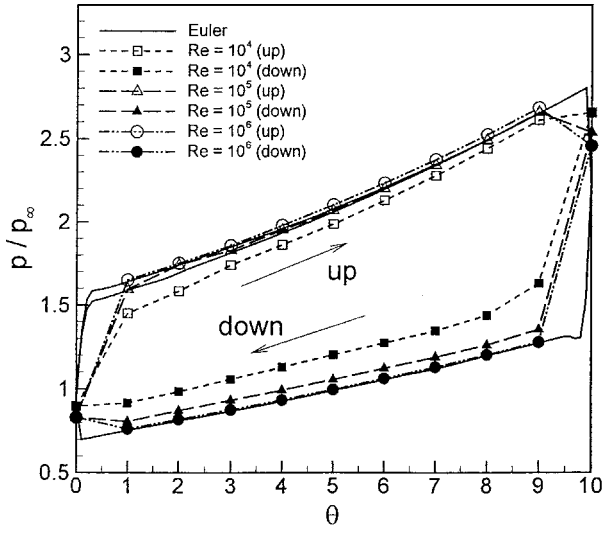

b) $s = 1.0$

Fig. 5 Effect of Reynolds number on surface pressure variation with wedge angle, $\bar{\Omega} = 0.1$.

different from that away from the corner mainly due to the evolution of separation bubble.

The unsteady pressure variations at $s = -0.028$ and at $s = 1.0$ when $\bar{\Omega} = 0.1$ are shown in Fig. 5 at various Reynolds numbers. The behavior of the flow in general is not much different from that observed in Fig. 4. The much larger difference between the pressure curves of the upward and downward phase than that for the case of $\bar{\Omega} = 0.01$ is due to the much faster ramp motion. We comment that the pressure hysteresis curve at $s = -0.028$ (Fig. 5a) was not established at the very first cycle in contrast to the case of $\bar{\Omega}$=0.01. It was at the second cycle of the ramp motion that the pressure curves shown in Fig. 5 was established.[12] Figure 5 illustrates also the effects of the Reynolds number on the pressure variation. At the point of $s = -0.028$, the pressure variation cycle for the case of $Re = 10^4$ lies above those for the cases of higher Reynolds numbers (Fig. 5a). This, we conjecture, is due to the viscid–inviscid interaction of the boundary layer over the flat plate region. The thicker boundary layer of the lower Reynolds number case causes the pressure to rise. Contrary to the pressure variation at the corner, the pressure variation curves at $s = 1.0$ (Fig. 5b) indicate that the pressure curve for $Re = 10^4$ lies inside the pressure curves for the cases of higher Reynolds numbers. The pressure during the upward motion is lower and the pressure during the downward motion is higher. This is an indication that the shock strength variation during the ramp motion for a smaller Reynolds number case is less than the variation for the case of a higher Reynolds number in accordance with the triple deck theory where the ramp angle scales as $Re^{1/4}\theta$. The effective wedge angle becomes smaller when the Reynolds number is small. As can be anticipated, the pressure curve for $Re = 10^6$ lies closest to the pressure curve of the Euler solution. It was found that the separation bubble appeared at a larger wedge angle when the Reynolds number was small, and the size of the separation bubble was always greater in the downward ramp motion than in the upward motion in all of the cases.[12]

Conclusions

Through a numerical study with a moving grid system, the unsteady viscous flow past a moving compression ramp was investigated for the cases of two reduced frequencies and three Reynolds numbers at Mach 3. Different from the Euler flow, the Navier–Stokes flow was not quasi steady at the reduced angular velocity of 0.01. Even at this small reduced frequency, the Navier–Stokes flow showed distinct unsteadiness caused by the evolution of separation bubble and its interaction with the outer flow. When the reduced angular velocity was 0.1, the isopressure lines indicated no distinguished signature of shock wave formation during the upward motion of the ramp. The shock wave started to appear after the ramp stop. The effect of Reynolds number was such that the shock strength increased with the Reynolds number. To examine the flow hysteresis, computations were carried out for the case of repeated ramp motion of a 0–10–0-deg cycle. The pressure hysteresis curves at the corner and at a point far from the corner on the wedge were given. It was found that these two curves behaved in an opposite manner. The pressure at the point far from the corner during the upward motion was much higher than the pressure during the downward motion as in the Euler flow. However, at the corner point, the pressure during the downward motion of the ramp was higher than the pressure during the upward motion.

Acknowledgments

The present work was financially supported in part through the BK-21 project and a grant from the Agency for Defense Development, Republic of Korea.

References

[1]Degani, D., and Steger, J. L., "Comparison Between Navier–Stokes and Thin-Layer Computations for Separated Supersonic Flow," *AIAA Journal*, Vol. 21, No. 11, 1983, pp. 1604–1606.

[2]Park, S. O., Chung, Y. M., and Sung, H. J., "Numerical Study of Unsteady Supersonic Compression Ramp Flows," *AIAA Journal*, Vol. 32, No. 1, 1994, pp. 216–218.

[3]Coon, M. D., and Chapman, G. T., "Experimental Study of Flow Separation on an Oscillating Flap at Mach 2.4," *AIAA Journal*, Vol. 33, No. 2, 1995, pp. 282–288.

[4]Carr, L. W., Chandrasekhara, M. S., and Brock, N. J., "Quantitative Study of Unsteady Compressible Flow on an Oscillating Airfoil," *Journal of Aircraft*, Vol. 31, No. 4, 1994, pp. 892–898.

[5]Hoffmann, K. A., and Chiang, S. T., *Computational Fluid Dynamics for Engineers*, Vol. 2, Engineering Education System, 1993, pp. 30, 31.

[6]Pulliam, T. H., "Time Accuracy and the Use of Implicit Methods," AIAA Paper 93-3360, 1993.

[7]Roe, P. L., "Approximate Riemann Solvers, Parameter Vectors and Difference Schemes," *Journal of Computational Physics*, Vol. 43, No. 2, 1981, pp. 357–372.

[8]Anderson, W. K., Thomas, J. L., and Van Leer, B., "Comparison of Finite Volume Flux Vector Splittings for the Euler Equations," *AIAA Journal*, Vol. 24, No. 9, 1986, pp. 1453–1460.

[9]Lewis, J. E., Kubota, T., and Lees, L., "Experimental Investigation of Supersonic Laminar, Two-Dimensional Boundary Layer Separation in a Compression Corner with and without Cooling," *AIAA Journal*, Vol. 6, No. 1, 1968, pp. 7–14.

[10]Burggraf, O. R., Rizzetta, D., Werle, M. J., and Vatsa, V. N., "Effect of Reynolds Number on Laminar Separation of a Supersonic Stream," *AIAA Journal*, Vol. 17, No. 4, 1979, pp. 336–343.

[11]Smith, F. T., and Khorrami, A. F., "The Interactive Breakdown in Supersonic Ramp," *Journal of Fluid Mechanics*, Vol. 224, 1991, pp. 197–215.

[12]Park, S. O., Lee, C. H., and Kang, K. M., "Naiver–Stokes Analysis of a Supersonic Flow over Moving Compression Ramp," AIAA Paper 2001-0568, 2001.

S. K. Aggarwal
Associate Editor

Modification of a Circular Cylinder Near Wake by a Rectangular Jet

D. M. Rooney* and M. S. Gaspin†
Hofstra University, Hempstead, New York 11549

Introduction

THE dynamics of a jet issuing into the wake behind various geometries in the presence of an upstream flow have been examined experimentally for a number of practical cases since Naudascher[1] first called attention to the phenomena occurring in the wakes of self-propelled bodies. Bradbury[2] contemporaneously measured the characteristics of turbulent plane jets exiting a thin slot at the trailing edge of an airfoil section, in the presence of an upstream flow of lower velocity than the jet. More recently, Serviente and Patel[3] have measured mean and turbulent velocity profiles behind an axisymmetric self-propelled body at various locations downstream of the jet nozzle. Several investigators have utilized less streamlined shapes as sources for the rear jet. Koutmos et al.[4] placed a square cylinder with a rear slot across a wind tunnel to determine the effect of injection ratio (jet to upstream velocity) on vortex shedding and recirculation patterns behind the square. Wood[5] employed an airfoil leading edge with an abrupt trailing edge and noted the effect of a jet on vortex formation and entrainment length of the shear layers. Zhdanov[6] followed by varying the width of the jet slot for a similar geometry.

Although wake phenomena behind circular cylinders in cross-flow have been examined thoroughly, there has been little effort to examine the effect of a rear jet on that well-known wake structure. Duke et al.[7] executed a water channel flow visualization study with a high-speed jet exiting a spanwise slot in a circular cylinder, but made no detailed measurements within the wake. Although experiments with axisymmetric jets behind models approximating to submarines, or with slotted jets behind airfoils that shed light on jet flap performance have more direct utility, nevertheless examination of the circular cylinder with rear-exiting jet can draw attention to similarities as well as differences in the response of bluff body wakes vis-à-vis streamlined body wakes in the presence of a jet. It is the purpose of the present Note to draw attention to the salient features of this particular jet–wake interaction.

Experimental Apparatus

Experiments were undertaken in a Hofstra University subsonic wind tunnel facility with a circular test section of 30.48-cm diam. Test cylinders with endplates spanned the tunnel width and featured a spanwise slot at midheight measuring $H = 25.4$ mm in length by $h = 0.635$ mm in width. A jet was produced by compressed air at 414 kPa (60 psi), and the jet flow was controlled by a regulator that produced volumetric flow rates ranging from 0 to 2400 l/h. The limited spanwise length of the slot necessarily produced a three-dimensional jet, the properties of which were measured along the major and minor axes at several locations downstream of the exit plane. Attention was primarily focused on data taken at the middle of the major axis of the slot because the mass flow rate of the jet was greatest around that height, thereby permitting the best comparison of the effect of a rear jet on a circular cylinder wake.

Two cylinders, one of $D = 6.35$ mm diameter and one of $D = 12.7$ mm diameter, were used during the test program. A minimum of nine test cases were run for each cylinder at two locations: three diameters and five diameters behind the central longitudinal axis of each of the cylinders. First the wake characteristics for an upstream velocity impinging on the cylinder with no rear jet were measured, then the wake produced by the jet alone at each of at least four jet flow rates employed, and then the wake produced by the jet in conjunction with the upstream flow at each of those jet flow rates. The upstream velocity was kept constant throughout the test program at $U_0 = 10.0$ m/s so that the Reynolds number based on cylinder diameter was either 4×10^3 or 8×10^3, for the smaller and larger cylinder, respectively. A nominal jet velocity V_j was obtained by dividing the volumetric flow rate as indicated on an Omega FL-210 flow meter by the cross-sectional area of the slot. Because of unsought differences in the machining of the slots, the jet profiles for the two cylinders differed. The smaller diameter cylinder produced a jet that was more concentrated at midheight, with little mass flow exiting at the upper and lower edges of the slot. Vertical scanning also showed some evidence of the saddlebacked velocity profiles that Quinn et al.[8] have documented to exist along the major axis of rectangular slots from which jets issue. For a representative flow rate, the velocity decreased along the major axis of the smaller cylinder to 50% of its maximum value over a 5-mm span and to 20% of its maximum value over an 8-mm span, when measured five diameters downstream of the cylinder axis. For the larger cylinder, the decrease to 50% of the maximum velocity occurred over a 14-mm span and to 20% of the maximum over a 22-mm span at five diameters downstream. At a comparable absolute distance downstream (three diameters for the larger cylinder being 31.7 mm from the slot, and five diameters downstream of the smaller cylinder measured 28.6 mm from the slot) the large cylinder velocity decreased to 50% over a 16-mm span and to 20% over a 22-mm span. Clearly the smaller cylinder jet was narrower vertically, but it expanded horizontally more rapidly at midheight. Despite these differences, it was decided to examine both cylinders because distinct jet structures would interact with a given cylinder wake, and any resulting dissimilarities in the combined flow wake could be analyzed in light of the given jet profile.

Both mean local velocity and turbulence intensity were measured at 1-mm intervals over a 40 mm length, 20 mm on either side of the cylinder center, using a hot-wire probe attached to a TSI Model 1054B constant temperature linearized anemometer. The temperature of the air jet and the wind-tunnel flow were measured by to be within 0.3°C of each other, so that no thermal biasing to the hot-wire readings occurred. Data passed through a filter to an rms voltmeter, which registered the rms fluctuations on the mean probe signal, and to an oscilloscope, where a visual signal was observed. A data acquisition system averaged and recorded readings for rms and mean velocity, and a Bruel–Kjaer spectrum analyzer monitored vortex shedding frequencies. Figure 1 shows the experimental setup.

Results and Discussion

The results are presented in dimensionless format with the relative magnitude of the jet characterized by a bleed coefficient $C_q = hV_j/DU_0$, the ratio of the jet flow rate to the rate of freestream flow through the same span H occupied by the slot, for a given diameter D. Distances behind and across the wake of the cylinder are nondimensionalized by the diameter. Hence, mean velocity and turbulence intensity profiles were constructed as a function of relative distance (z/D) across the cylinder wake at streamwise distances $x/D = 3$ and 5. The 95% confidence interval in mean freestream

Received 24 July 2002; revision received 16 September 2002; accepted for publication 16 September 2002. Copyright © 2002 by the American Institute of Aeronautics and Astronautics, Inc. All rights reserved. Copies of this paper may be made for personal or internal use, on condition that the copier pay the $10.00 per-copy fee to the Copyright Clearance Center, Inc., 222 Rosewood Drive, Danvers, MA 01923; include the code 0001-1452/03 $10.00 in correspondence with the CCC.

*Associate Professor, Department of Engineering. Member AIAA.
†Undergraduate Research Assistant, Department of Engineering; currently Undergraduate Student, Department of Mechanical and Aerospace Engineering, Cornell University, Ithaca, NY 14853.